ARCHIVES
of
FOUNDRY ENGINEERING

ISSN (2299-2944)

10.24425/afe.2025.155348

Published quarterly as the organ of the Foundry Commission of the Polish Academy of Sciences

Corrosion Behaviour of 316 Stainless Steel in Molten CaCl2-CaF2-CaO Salts at High Temperature

P. Palimąka *, B. Leszczyńska-Madej
AGH University of Krakow, Poland
* Corresponding author: e-mail: palimaka@agh.edu.pl

Received 29.01.25; accepted in revised form 22.04.25; available online 11.06.2025

Abstract

One of the major limitations of using molten salts for CO_2 capture processes from industrial gas streams is the availability of construction materials with adequate corrosion resistance. This is due to the high operating temperature of the process and the aggressive environment of chloride-fluoride molten salts. In this study, the influence of temperature and a molten, eutectic mixture of $CaCl_2$ - CaF_2 with the addition of 10 wt.% CaO on the behavior of SS316 steel was evaluated. Tests were conducted at 700 °C and 950 °C for 40, 80, and 120 hours. Material samples were weighed before and after the tests, and selected samples underwent microscopic analysis (SEM, EDS), measurements of the corrosion product layer thickness, and wall thickness. The corrosion rate of SS316 steel was also determined. The results showed, among other findings, that at 700 °C, mass losses were minimal (max. 0.5%), and the corrosion layer had an average thickness not exceeding 8.2 µm. At 950 °C, mass loss increased to 3.85%, and the corrosion product layer reached an average thickness of 83 µm. Intergranular corrosion was also observed, along with enrichment of the corrosion layer with salt elements (Ca, O, Cl) and steel alloying elements (Cr, Ni). Additionally, segregation of Cr, Mn, and Mo was noted at grain boundaries. The calculated corrosion rate of SS316 steel at 700 °C was 171 µm/year, while at 950 °C, it was significantly higher at 1540 µm/year.

Keywords: Molten salts, SS316 corrosion, CO_2 capture in molten salts

1. Introduction

Molten salts, due to their specific properties such as high heat capacity, good thermal conductivity, and chemical stability over a wide temperature range, are used in many industrial and technological sectors. Their most common applications include solar energy, nuclear reactors, metallurgy, and energy storage. In CSP (Concentrated Solar Power) installations, molten salts are used as a medium for storing thermal energy [1, 2]. Such installations can be employed in heating and industrial systems as heat-accumulating reservoirs. Molten salts can also serve as a coolant in next-generation nuclear reactors, such as MSRs (Molten Salt Reactors) [3, 4]. In these reactors, they act as both a coolant and a medium for transporting nuclear fuel, enhancing both safety and energy efficiency. In thermal processing, molten salts are used for quenching, carburizing, or brazing. In furnaces, they create a homogeneous thermal environment, enabling uniform heat treatment of metals and alloys [5, 6]. One of the most common uses of molten salts is in metallurgical processes utilizing electrolysis to produce aluminum, lithium, sodium, potassium, and magnesium [7, 8], as well as in recycling, such as secondary smelting of aluminum and its alloys [9]. In all these applications, one of the greatest technological challenges is the development of construction materials for tanks, pumps, pipelines, valves, and other components operating at high temperatures and in continuous contact with molten salts of varying compositions (chlorides, fluorides, nitrates, carbonates, etc.). Research on materials capable of withstanding such aggressive conditions continues, primarily focusing on two groups of metallic materials: steels (e.g., SS316 [10], SS316L [11], SS304 [12]) and high-nickel alloys [12-14].

One of the new, potentially attractive applications of molten salts is their use in the process of capturing CO_2 from industrial plant gases. This enables the rapid and efficient reduction of CO_2 emissions at the source of its generation [15, 16]. To date, this technology has been extensively studied under laboratory conditions, and a prototype reactor for CO_2 capture has been constructed [17]. The construction material for key components (reactor, sparging lances, transport pipes) was technical nickel, Ni 200 alloy. The authors conducted preliminary, long-term (800-hour) tests of CO_2 absorption and desorption from a synthetic gas mixture of N_2 and 15 vol.% CO_2, as well as an evaluation of the wear of individual reactor components. It was found that technical nickel, when operating at temperatures up to 950°C in the aggressive environment of molten salts ($CaCl_2$-CaF_2-CaO), exhibits significant grain growth and intergranular corrosion [17]. As a result, there is material loss in components in constant contact with molten salts, along with changes in the geometry of structural elements (thinning). The authors of this article evaluated the material wear of a group other than nickel alloys, specifically austenitic steel SS316.

2. Materials and methods

The material used for the study was SS316 steel, with its composition presented in Table 1.

Table 1.
Nominal chemical composition (% by weight) of SS316, as provided by the vendor.

Comp.	C	Si	Mn	Ni	Cr	Mo	Cu	Fe
[% wt.]	0.024	0.6	0.98	10.13	16.77	0.024	0.1	Bal.

Six samples were prepared for the study, cut from a tube with an outer diameter of 8.1 mm and a wall thickness of 0.96 mm, as shown in Figure 1. The samples were washed in 1M NaOH solution, cleaned using acetone, and dried in warm air. The samples were stored in vacuum desiccator to avoid oxidation/corrosion before testing. The weight of the samples was recorded before corrosion test. Metal samples were tested in ceramic (alundum) crucibles (12 cm height, 6.0 cm diameter, and 2 mm wall thickness). Each crucible contained 120.0 g of $CaCl_2$-CaF_2-CaO (12.0 g CaO, 108.0 g eutectic $CaCl_2$-CaF_2 molten salt with 86.2/13.8 wt. %, dried at 300 °C for over 48 hours), resulting in a salt height of about 3 cm after melting. During the test, the samples were completely immersed in the molten salt. Corrosion tests were conducted in a Nabertherm muffle furnace. After 40, 80, and 120 hours, the furnace was opened, the crucible was placed on a preheated ceramic brick, and the sample was carefully extracted using tongs (Figure 2).

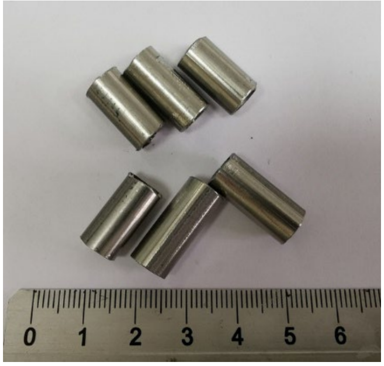

Fig. 1. SS316 samples prepared for testing

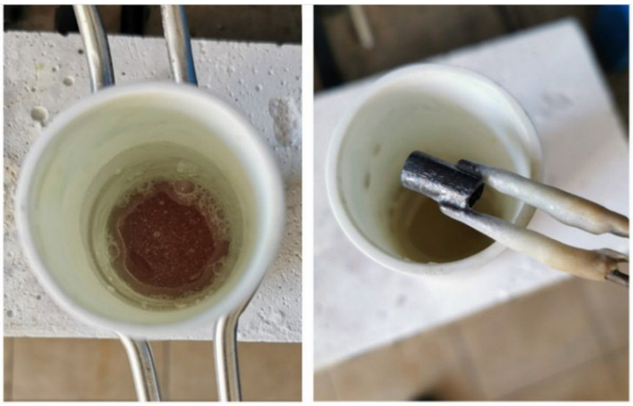

Fig. 2. Crucible with molten salt (left) and the SS316 steel sample immediately after being removed from the molten salts

After reaching room temperature, each sample was rinsed with distilled water to remove residual salts, dried, and weighed. Microscopic observations and analyses were performed on the samples with the maximum exposure time to high temperature and molten salts, i.e., after 120 hours. The tests were conducted at two temperatures (700°C and 950°C), corresponding to the conditions during CO_2 absorption and desorption processes in the molten salt CO_2 capture method [17]. Cross-sectional observations of the samples were carried out using light microscopy and scanning electron microscopy (SEM) techniques, accompanied by chemical composition analysis in microareas using SEM/EDS. Samples for microscopic analysis were embedded in Epofix Kit resin and conductive PolyFast resin. The prepared samples were then subjected to grinding (using abrasive papers with successive grit sizes: 220, 500, 800, 1200, 2000, and 4000) and two-step mechanical polishing following the Struers procedure. This involved using Dia Duo diamond paste suspension with a grain size of 3 μm and OPS colloidal silica suspension for final polishing with a grain size of 0.25 μm. The samples were not etched. Microstructure observations were conducted using an Olympus GX51 light microscope equipped with digital image recording and a Hitachi SU 70 scanning electron microscope. Images were captured using secondary electron (SE) and backscattered electron (BSE) detectors. The chemical composition of the corrosion product layer was analyzed, and its thickness was determined. The XRD analysis was performed using a Rigaku MiniFlex II device

The corrosion rate (*CR*) was estimated by assessing weight loss using the relation (1) presented in Ding et al. [18].

$$CR = \frac{\Delta m}{\rho A} \cdot \frac{365 \cdot 24}{t} \cdot 10^4 \quad (1)$$

where: *CR* [$\mu m \cdot year^{-1}$] - corrosion rate, Δm [g] - loss of sample mass during testing, ρ [$g \cdot cm^{-3}$] - sample density, A [cm^2] - initial area of the sample and t [h] - time.

4. Results

The results of the mass measurements for the samples tested at 700°C and 950°C are presented in Table 2.

Table 2.
Results of sample mass measurements after tests at 700°C

Temp. °C	Time, h	Mass of the sample before the experiment, g	Mass of the sample after the experiment, g	Mass change, %
700	40	2.489	2.485	0.16
	80	3.105	3.096	0.29
	120	2.624	2.611	0.50
950	40	2.768	2.728	1.45
	80	3.256	3.169	2.67
	120	2.520	2.423	3.85

It was found that the mass loss of samples kept in molten salts at a temperature of 700°C did not exceed 0.5% of their initial mass. Significantly greater mass changes occurred at 950°C, reaching up to 3.85% after 120 hours. The initial sample was subjected to microscopic observations and wall thickness measurements. An example of a thickness measurement is shown in Figure 3b.

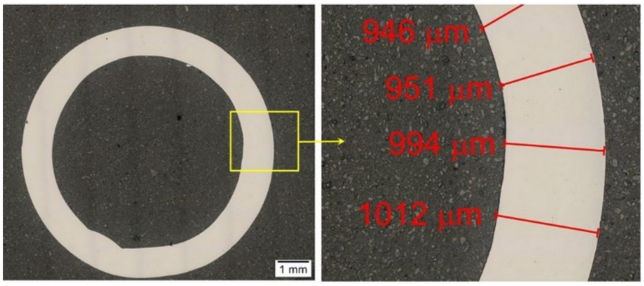

a) b)

Fig. 3. Macro image of the sample before testing (a) and microstructure with an example of wall thickness measurement (b), unetched cross-section, light microscopy

Meanwhile, Figure 4 shows the microstructure image of the initial sample.

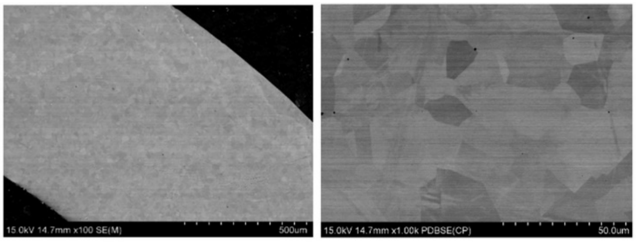

a) b)

Fig. 4. Microstructure of the sample cross-section before testing: a) magnification 100x, b) magnification 1000x; SEM

The microstructure of the SS316 sample consists of regular austenite grains with sizes ranging from 20 to 40 µm. No large intermetallic phase inclusions or carbides were observed.
Figure 5 presents a macro image of the sample after 120 hours of exposure to molten salts at 700°C, along with an example of a wall thickness measurement.

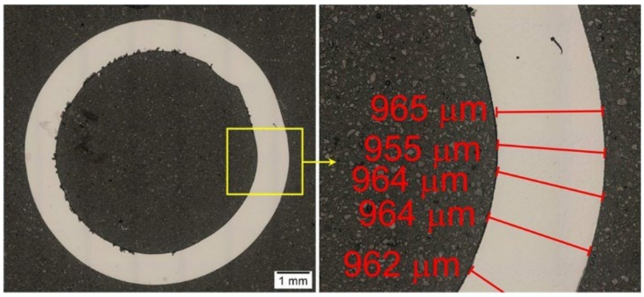

a) b)

Fig. 5. Macro image of the sample after tests at 700°C (120 h) (a) and microstructure with an example of wall thickness measurement (b), unetched cross-section

Meanwhile, Figure 6 shows microstructure images captured using a scanning electron microscope.

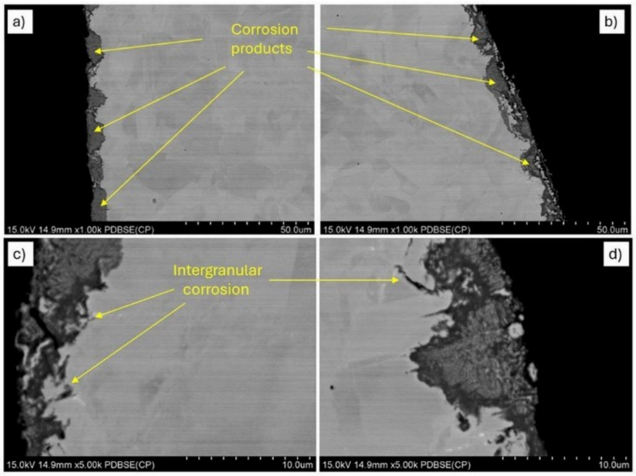

Fig. 6. Microstructure of the sample after tests at 700°C (120 h): a) magnification 5000x, b) magnification 1000x; c) magnification 5000x, d) magnification 5000x; SEM

The results obtained demonstrated the presence of a non-uniform corrosion product layer on both sides of the sample (inner and outer surfaces) (Figure 6a and Figure 6b). Additionally, evidence of intergranular corrosion propagating from the corrosion product layer into the metallic material was observed (Figure 6c and Figure 6d).

Figure 7 presents the results of the analysis of a fragment of the sample's microstructure after 120 hours of testing at 700°C, including a section of the sample and the corrosion product layer formed on it.

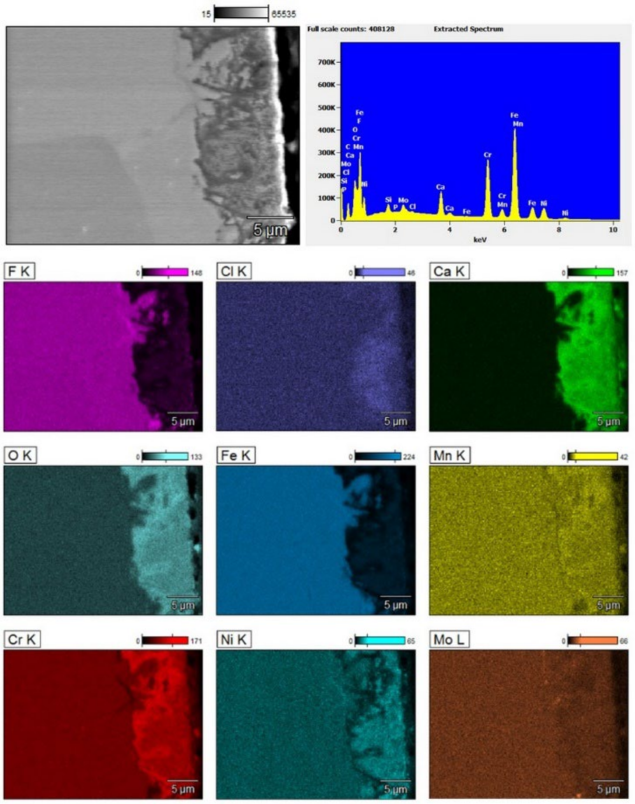

Fig. 7. Microstructure of the sample tested for 120 h at 700°C and elemental distribution maps of components present in the molten salts: F, Cl, Ca, O, as well as primary alloying elements of AISI 316 steel: Fe, Mn, Cr, Ni, Mo

The results of the chemical composition analysis in microareas, presented as elemental distribution maps (Figure 7), indicate an enrichment of the corrosion layer with Cl, Ca, and O. These elements originate from the molten salts in continuous contact with the tested material. Additionally, at the interface between the corrosion layer and the metallic material, segregation of alloying elements such as Cr and Mn, as well as enrichment in O, was observed. Furthermore, the corrosion product layer exhibited increased Ni and Cr content compared to the base material. This suggests chemical reactions between these elements and the molten salts, leading to the formation of solid corrosion products on the surface of the tested material. These observations are confirmed by the results of linear analysis, as shown in Figure 8.

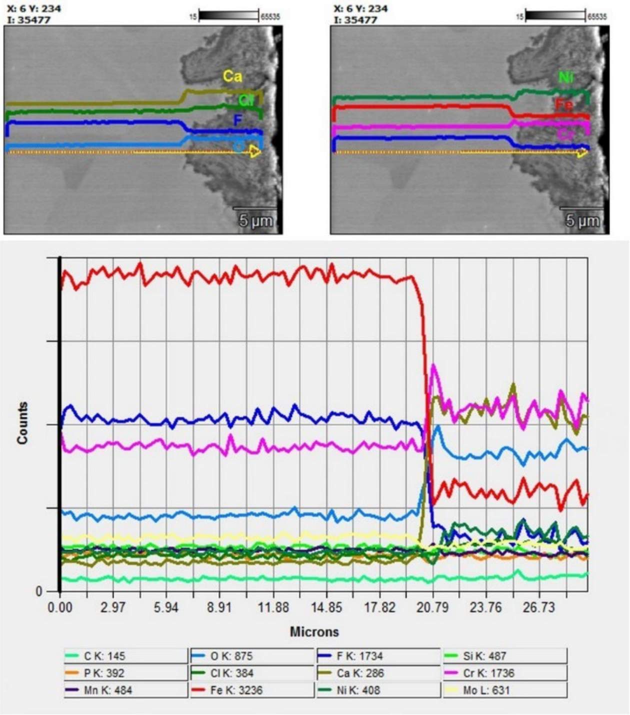

Fig. 8. Results of linear analysis of the microstructure area (sample tested for 120 h at 700°C) on a cross-section containing the corrosion product layer and the base material; SEM

The sample tested at 950°C for 120 hours was also subjected to microscopic observations and wall thickness measurements (Figure 9a and Figure 9b). Meanwhile, Figure 9c presents a view of a fragment of the sample with a visible corrosion product layer.

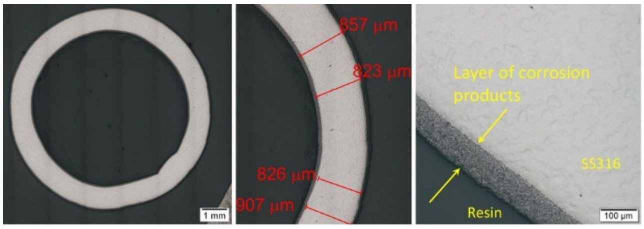

a) b) c)

Fig. 9. Macro image of the sample after tests at 950°C (120 h) (a), microstructure with an example of wall thickness measurement (b), and the appearance of the corrosion product layer with a fragment of SS316 (c). Unetched cross-section, light microscopy

The example measurements shown in Figure 9b indicate significant thinning of the sample wall compared to the material before the experiments. Meanwhile, the cross-sectional image presented in Figure 9c reveals the presence of a relatively thick corrosion product layer on the surface of the analyzed material. Figures 10 and 11 display microstructure images of the sample and elemental distribution maps obtained using SEM.

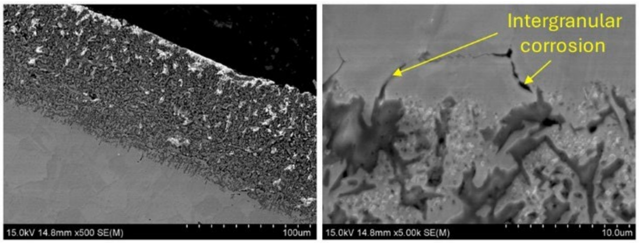

a) b)

Fig. 10. Microstructure of the sample tested for 120 h at 950°C; image (a) shows the morphology of the corrosion layer, and image (b) displays evidence of intergranular corrosion; SEM

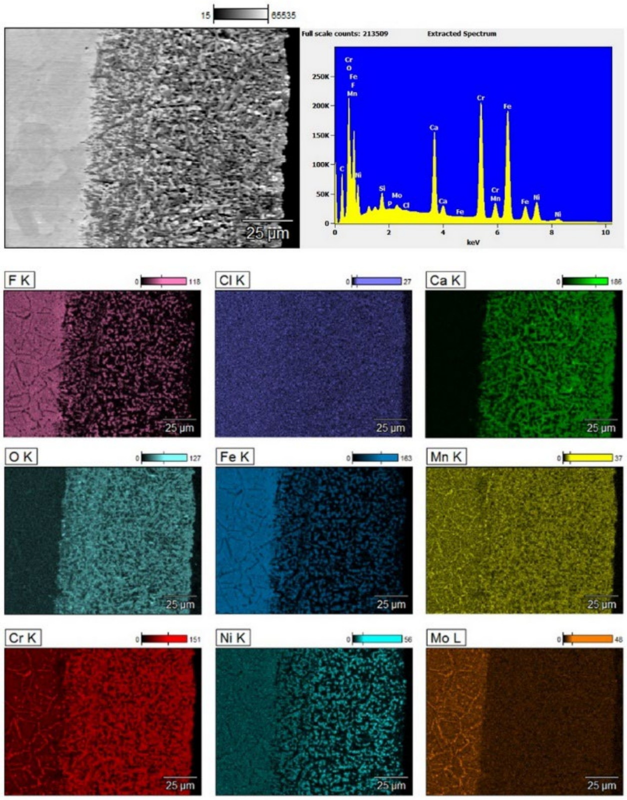

Fig. 11. Microstructure of the sample tested for 120 h at 950°C and elemental distribution maps of components present in the molten salts: F, Cl, Ca, O, as well as primary alloying elements of SS316 steel: Fe, Mn, Cr, Ni, Mo

The cross-sectional images shown in Figure 11 indicate the presence of a corrosion layer uniformly distributed on the surface of the tested sample. The transition between the sample material and the corrosion product layer is continuous. The layer consists of micro-areas differentiated in terms of chemical composition and exhibits a "spongy" morphology. Additionally, localized traces of intergranular corrosion spreading from the scale into the material were observed (Figure 10b).

The results of the chemical composition analysis in microareas, presented as elemental distribution maps (Figure 11) and linear analysis (Figure 12), demonstrate enrichment of the layer with Ca and O.

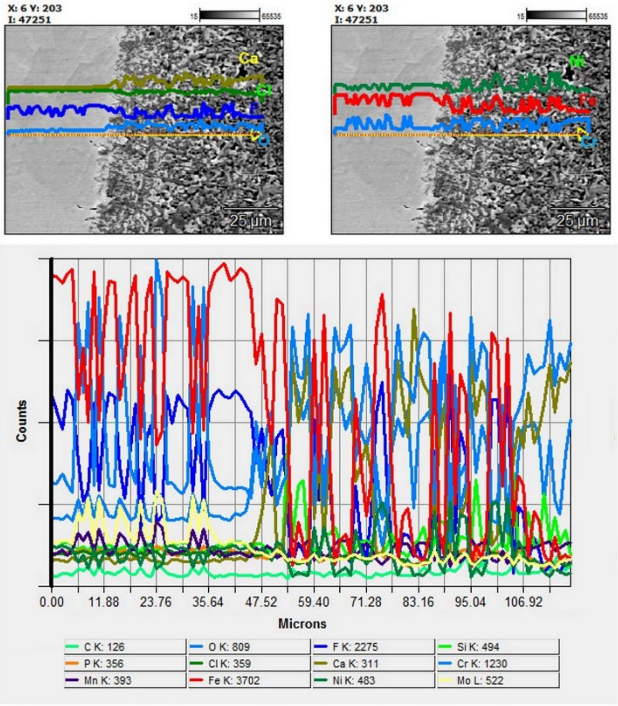

Fig. 12. Results of linear analysis of the microstructure area of the sample tested for 120 h at 950°C, showing a cross-section containing the corrosion layer and the tube material; SEM

Additionally, segregation of Cr, Mn, and Mo to the grain boundaries in the tube was observed, which may reduce the material's corrosion resistance. The corrosion layer is multi-component, as confirmed by the EDS chemical composition analysis results. Furthermore, some micro-areas in the sample are enriched in Ni and Cr. These observations are corroborated by the results of the linear elemental analysis (Figure 12). The thickness measurements of the walls of the tested samples, both before and after testing at 700°C and 950°C for 120 hours, as well as the thickness of the scale formed on the samples, are summarized in Table 3.

Table 3.
Results of measurements of the wall thickness and corrosion layer thickness of samples after tests at 700 °C and 950 °C

Temp., °C	Wall thickness, μm	Thickness of corrosion layer, μm
Sample before tests	Min: 932	-
	Max: 1013	-
	Average: 967	-
700	Min: 918	Min: 5.2
	Max: 1006	Max: 14
	Average: 954	Average: 8.2
950	Min: 807	Min: 66
	Max: 907	Max: 99
	Average: 853	Average: 83

The average values were calculated from 24 measurements taken at different points on the sample. The thickness measurement results indicate that the difference in the wall thickness of the tested samples before and after the tests strongly depends on the temperature. At 700°C, the thickness reduction (wall thinning) was 1.34%, while at 950°C, this value reached 11.8%. Similarly, the thickness of the corrosion layer is approximately 10 times greater in the sample exposed to higher temperatures.

Figure 13 presents the results of the phase composition analysis of the corrosion products formed on the sample surface at a temperature of 950 °C after 120 hours of contact with molten salts.

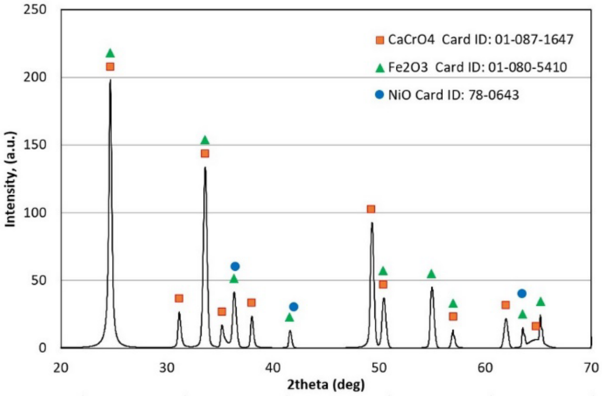

Fig. 13. XRD pattern of the corrosion products formed at 950 ºC on the surface of SS316

The results of the XRD analysis indicate the presence of metal oxides, which suggests the possibility of reactions occurring between the alloying elements of SS316 and the components of the molten salts or the furnace atmosphere.

The final stage of the study was the calculation of the corrosion rate. Table 4 provides a summary of the calculated values of this parameter.

Table 4.
Results of the corrosion rate (*CR*) calculations for the tested material at 700°C and 950°C

Temp., ºC	Time, h	*CR*, µm/year	*CR* (average), µm/year	SD, µm/year
700	40	160	171	10
	80	180		
	120	173		
950	40	1596	1540	228
	80	1736		
	120	1290		

The corrosion rate (*CR*) values calculated using Equation (1) and the mass changes of the samples (Table 2) after 40, 80, and 120 hours at 700°C are similar. In contrast, at the higher temperature of 950°C, the scatter in the obtained results is significantly larger. This may be due to incomplete removal of crystallized salts from the surface of some samples. Nevertheless, the average *CR* values obtained for the tested temperatures differ by an order of magnitude, indicating a strong acceleration of corrosion caused by high temperature. These *CR* calculations, based on laboratory test results, assume a constant corrosion rate at a given temperature.

4. Discussion

The mechanism of high-temperature corrosion in a chlorine-containing environment is not fully understood. However, it is believed [19] that the accelerated corrosion of steel in a high-temperature, chlorine-containing environment is mainly due to the lower melting and boiling points of chlorides present in the corrosion products compared to the corresponding metal oxides. One of the models used to interpret corrosion in chloride salts is the active oxidation model [20], which, in relation to the system studied in this work, is schematically illustrated in Figure 14.

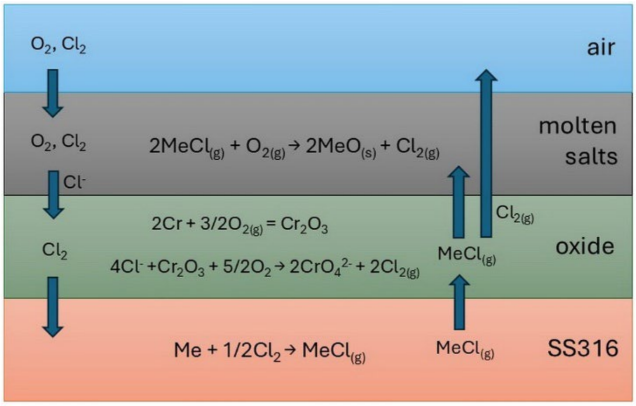

Fig. 14. Schematic diagram of activated oxidation.

In the investigated experimental system, gaseous Cl_2, and O_2 may be present. As a result of oxidation reactions (2), (3), and (4), the respective metal oxides could be formed, with the formation of Cr_2O_3 being the most favored reaction [21]:

$$2Ni + O_2 = 2NiO \quad (2)$$

$$2Fe + 3/2O_2 = Fe_2O_3 \quad (3)$$

$$2Cr + 3/2O_2 = Cr_2O_3 \quad (4)$$

Apart from metal oxidation reactions, the oxygen present in the furnace atmosphere during the experiments can react with chloride ions (Cl^-) from the molten salts, forming gaseous chlorine according to reaction (5):

$$4Cl^-(l) + O_2(g) \rightarrow 2Cl_2(g) + 2O^{2-}(l) \quad (5)$$

Chlorine can react with metals such as Ni, Fe and Cr. However, as demonstrated in Figure 15, the formation of $CrCl_3$ is the most favored reaction due to its most negative Gibbs free Energy (calculated based on the HSC Chemistry 7.0 software).

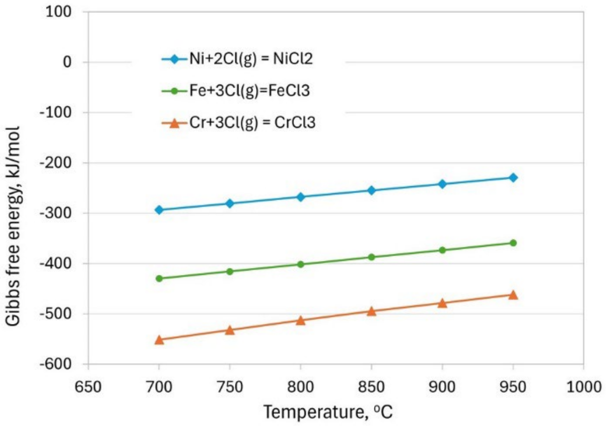

Fig. 15. The Gibbs free energy for the formation reaction of Ni, Fe and Cr chlorides in the temperature range of 700-950°C [22]

The formed $CrCl_3$, $FeCl_3$, and $NiCl_2$ can diffuse to the surface of the molten salt/oxide layer, where they react with O_2 according to the following equations:

$$2NiCl_2 + O_2 = 2NiO + 2Cl_2 \quad (6)$$

$$2CrCl_3 + 3/2O_2 = Cr_2O_3 + 3Cl_2 \quad (7)$$

$$2FeCl_3 + 3/2O_2 = Fe_2O_3 + 3Cl_2 \quad (8)$$

Due to the highest vapor pressure of $CrCl_3$ [20] and the most negative standard Gibbs free energy associated with the formation of Cr_2O_3, reaction (7) will proceed preferentially. The resulting Cl_2 will then diffuse through cracks and pores in the oxide layers back to the oxide/metal phase boundary, where it will react with the metal again. Reaction (9) is also possible. The formation of $CaCrO_4$ was corroborated by XRD analysis of the corrosion products, as shown in Figure 13.

$$2CaCl_2 + Cr_2O_3 + 5/2O_2(g) = 2CaCrO_4 + 2Cl_2(g) \quad (9)$$

Analysis of wall thickness and corrosion layer measurements confirmed that the intensity of corrosion processes increases significantly with rising temperature. Samples exposed to molten salts at 700°C showed minor wall thickness reductions (1.34%) and a relatively thin corrosion product layer.

The observed segregation of Cr, Mn, and Mo (local increase in the concentration of these elements at grain boundaries), as shown in Fig. 11, may lead to the initiation of corrosion or cracking due to the formation of stresses. This type of corrosion is one of the most common in molten salt environments [21]. However, overall degradation was relatively minimal. Such esistance of SS316 steel at lower temperatures indicates its potential applicability in processes requiring moderate thermal conditions. In the context of using SS316 for constructing components in CO_2 capture devices in molten salts, these conditions prevail in the absorber, where the CO_2 absorption temperature does not exceed 700°C.

At higher temperatures (950 °C), the material degradation was significantly more advanced. Wall thinning reached 11.8%, indicating an intensification of corrosion processes. The corrosion layer thickness was ten times greater compared to samples tested at the lower temperature. Intergranular corrosion was also observed, with a tendency to propagate into the material.

Corrosion rate values calculated based on the mass loss of samples showed a difference of an order of magnitude between the tested temperatures (700°C and 950°C). The mass change suggests that corrosion products, being in continuous contact with the molten salts, either dissolve in them or detach mechanically, causing their contamination. This may alter the chemical composition of the salts and reduce the overall efficiency of the absorption/desorption process.

The otained research results indicate that using SS316 steel in high-temperature conditions is not a suitable solution, as accelerated corrosion could limit the durability of structural components in such environments. This highlights the need for further development of construction materials capable of withstanding the aggressive environmental conditions in the molten salt CO_2 capture technology using $CaCl_2$-CaF_2-CaO.

5. Conclusions

The analysis of the obtained research results allows for the following conclusions:

- SS316 steel undergoes surface and intergranular corrosion under the influence of molten salts $CaCl_2$-CaF_2-CaO and high temperatures (700°C and 950°C).
- At 700°C, after 120 hours of testing, the mass loss of samples is minimal, not exceeding 0.5%, while at 950°C, it reaches 3.85%.
- The corrosion layer consists of various phases with a "spongy" morphology and is enriched with elements both from the molten salts (Ca, O) and from the steel alloy (Cr, Ni, Fe).
- Due to high temperatures and the aggressive molten salt environment, intergranular corrosion is observed, propagating from the corrosion layer into the material, potentially weakening the steel structure.
- The thickness of the corrosion product layer is over 10 times greater at 950°C (83 μm) compared to the layer formed at 700°C (8.2 μm).
- The average corrosion rate of SS316 steel is 171 μm/year at 700°C and 1540 μm/year at 950°C.
- SS316 steel exhibits minimal, acceptable wear in the tested molten salt environment at 700°C and can be considered for the construction of structural elements (e.g., lances, shields, sensors) in a CO_2 absorber where the operating temperature does not exceed 700°C.
- For constructing components with complex geometries exposed to continuous contact with molten salts (e.g., pumps, valves, flanges), where installation tightness is required, SS316 steel is unsuitable as a construction material, even at 700°C.
- SS316 steel is not recommended for the construction of CO_2 desorber components, where the operating temperature is 950°C.

Acknowledgements

The research leading to these results has received funding from the Norway Grants 2014–2021 via the National Centre for Research and Development. The results are part of the Polish–Norwegian project: Carbon Capture in Molten Salts—Prototype, acronym CCMS-P, registration number NOR/POLNORCCS/CCMS-P/0004/2019-00.

References

[1] Tang, Z. & Tao, W.Q. (2023). Strength analysis of molten salt tanks for concentrating solar power plants. *Energy Storage and Saving.* 2(4), 571-577. DOI: 10.1016/j.enss.2023.08.003.

[2] Russo, V., Petroni, G., Rovense, F., Giorgetti, M., Napoli, G., Giorgi, G. & Gaggioli, W. (2025). Experimental testing results on critical components for molten salt-based CSP systems. *Energies.* 18(1), 198, 1-21. DOI: 10.3390/en18010198.

[3] Serp, J., Allibert, M., Beneš, O., Delpech, S., Feynberg, O., Ghetta, V., Heuer, D., Holcomb, D., Ignatiev, W., Kloosterman, J.L., Luzzi, L., Merle-Lucotte, E., Uhlíř, J., Yoshionka, R. & Zhimin, D. (2014). The molten salt reactor (MSR) ingeneration IV: Overview and perspectives. *Progress in Nuclear Energy.* 77, 308-319. https://doi.org/10.1016/j.pnucene.2014.02.014.

[4] Noori-Kalkhoran, O., Jain, L. & Merk, B. (2024). On the use of a chloride or fluoride salt fuel system in advanced molten salt reactors, part 3; radiation damage. *Energies (Basel).* 17(19), 4772, 1-14. DOI: 10.3390/en17194772.

[5] Arcos, C., Guerra, C., Ramos-Grez, J.A. & Sancy, M. (2023). Ni-Al bronze in molten carbonate manufactured by LPBF: effect of porosity design on mechanical properties and oxidation. *Materials.* 16(10), 3893, 1-15. DOI: 10.3390/ma16103893.

[6] Quadros, J.D., Khan, S.A., Mohin, M., Mogul, Y.I., Aabid, A., Baig, M. & Ahmed, O.S. (2023). Heat transfer of Ca (NO3)2-KNO3 molten salt mixtures for austempering and martempering processes of steels. *ACS Omega*. 9(15), 17266-17275. DOI: 10.1021/acsomega.3c10262.

[7] Zhang, J., Yan, H., Liu, Z., Guo, S., Yang, Y., Yang, G., Xia,R., Hu, M. & Li, L. (2024). Progress in research and application of molten salt electrolysis for titanium extraction. *Journal of Electrochemical Society.* 171(8), 082502, 1-16. DOI: 10.1149/1945-7111/ad6d95.

[8] Pietrzyk, S., Palimąka, P. & Gębarowski, W. (2014). The effect of liquid aluminium on the corrosion of carbonaceous materials. *Archives of Metallurgy and Materials*. 59(2), 545-550. DOI: 10.2478/amm-2014-0090.

[9] Palimąka, P. (2020). Thermal cleaning and melting of fine aluminium alloy chips. *Archives of Foundry Engineering.* 20(4), 91-96. DOI: 10.24425/afe.2020.133353.

[10] Zhu, M., Zeng, S., Zhang, H., Li, J. & Cao, B. (2018). Electrochemical study on the corrosion behaviors of 316 SS in HITEC molten salt at different temperatures. *Solar Energy Materials and Solar Cells.* 186, 200-207 DOI: 10.1016/J.SOLMAT.2018.06.044.

[11] Abu-Warda, N., García-Rodríguez, S., Torres, B., Utrilla, M.V. & Rams, J. (2024). Effect of Molten Salts Composition on the Corrosion Behavior of Additively Manufactured 316L Stainless Steel for Concentrating Solar Power. *Metals (Basel).* 14(6), 639, 1-18. DOI: 10.3390/met14060639.

[12] Sandhi, K.K. & Szpunar, J. (2021). Analysis of corrosion of hastelloy-N, alloy x750, SS316 and SS304 in molten salt high-temperature environment. *Energies (Basel).* 14(3), 543, 1-10. DOI: 10.3390/en14030543.

[13] Feng, J., Gao, J., Mao, L., Bedell, R. & Liu, E. (2024). Modeling the impact of grain size on corrosion behavior of Ni-based alloys in molten chloride salt via cellular automata. *Metals.* 14(8), 931, 1-12. DOI: 10.3390/met14080931.

[14] Kettrakul, P., Siripongsakul, T., Kanjanaprayut, N., Wiman, P., Promdirek, P. (2023). *Effect of Si addition in NiCrAl coating on corrosion in molten nitrate salt*. Retrieved January 28, 2025, from https://doi.org/10.21203/rs.3.rs-3282513/v1.

[15] Olsen, E. & Tomkute, V. (2013). Carbon capture in molten salts. *Energy Science & Engineering.* 1(3), 144-150. DOI: 10.1002/ese3.24.

[16] Tomkute, V., Solheim, A. & Olsen, E. (2014). CO_2 capture by CaO in molten CaF_2-$CaCl_2$: Optimization of the process and cyclability of CO2 capture. *Energy and Fuels.* 28(8), 5345-5353. DOI: 10.1021/ef5010896.

[17] Palimąka, P., Pietrzyk, S., Balcerzak, M., Żaba, K.,Leszczyńska-Madej, B. & Jaskowska-Lemańska, J. (2024). Evaluation of the wear of Ni 200 alloy after long-term carbon capture in molten salts process. *Materials*. 17(24), 6302, 1-25. DOI: 10.3390/ma17246302.

[18] Ding, W., Bonk, A. & Bauer, T. (2018). Corrosion behavior of metallic alloys in molten chloride salts for thermal energy storage in concentrated solar power plants: A review. *Frontiers of Chemical Science and Engineering*. 12, 564-576. DOI: 10.1007/s11705-018-1720-0.

[19] Ma, H. (2003). *Corrosion of Metallic Materials in High-temperature Chloride Salt Environment*. Level of Thesis, Dalian University of Technology, Dalian, China.

[20] Wang, M., Song, Z., Huihui, Z. Zhu, M., Chengxin, L. & Boshuai. L. (2020). Corrosion behaviors of 316 stainless steel and Inconel 625 alloy in chloride molten salts for solar energy storage. *High Temperature Materials and Processes*. 39(1), 340-350. DOI: 10.1515/htmp-2020-0077.

[21] Wei, Y., La, P., Zheng, Y., Zhan, F., Yu, H., Yang, P., Zhu, M., Bai, Z. & Gao, Y. (2025). Review of molten salt corrosion in stainless steels and superalloys. *Crystals.* 15(3), 237, 1-33. DOI: 10.3390/cryst15030237.

[22] HSC Chemistry v 7.0, Outotec Research